J|A|C|S
ARTICLES

Published on Web 01/19/2010

Mechanism of Water Oxidation by Single-Site Ruthenium Complex Catalysts

Javier J. Concepcion,[‡] Ming-Kang Tsai,[†] James T. Muckerman,[†] and Thomas J. Meyer*[,‡]

Department of Chemistry, University of North Carolina at Chapel Hill, Chapel Hill, North Carolina 27599, and Chemistry Department, Brookhaven National Laboratory, Upton, New York 11973-5000

Received June 20, 2009; E-mail: tjmeyer@email.unc.edu

Abstract: The mechanism of Ce(IV) water oxidation catalyzed by $[Ru(tpy)(bpm)(OH_2)]^{2+}$ (tpy = 2,2′:6′,2″-terpyridine; bpm = 2,2′-bipyrimidine) and related single-site catalysts has been determined by a combination of mixing and stopped-flow experiments with spectrophotometric monitoring. The mechanism features O---O coupling by water attack on $Ru^{V}{=}O^{3+}$ and three peroxidic intermediates that have been characterized by a combination of spectroscopy and DFT calculations.

Introduction

Water oxidation catalysis occurs in biology in photosystem II (PSII) by single-photon, single-electron activation of multielectron catalysis in the oxygen-evolving complex (OEC).[1−4] The first reported molecular catalyst for water oxidation was the ruthenium blue dimer, *cis,cis*-$[(bpy)_2(H_2O)Ru^{III}ORu^{III}(OH_2)(bpy)_2]^{4+}$ ($[(H_2O)Ru^{III}ORu^{III}(OH_2)]^{4+}$, bpy = 2,2′-bipyridine).[5−8] It undergoes stepwise electron−proton loss to give a reactive $[(O)Ru^{V}ORu^{V}(O)]^{4+}$ intermediate. Once formed, $[(O)Ru^{V}ORu^{V}(O)]^{4+}$ undergoes water attack at an oxo group to give an intermediate peroxide followed by further oxidation and O_2 evolution.[9] Complications arise in catalytic cycles from anation which, so far, has limited the use of the blue dimer as a water oxidation catalyst.

Other molecular catalysts for water oxidation have been reported recently, including examples of ruthenium and iridium complexes, but without detailed mechanistic insight.[10−13] We recently reported catalytic water oxidation by the single-site catalysts $[Ru(tpy)(bpm)(OH_2)]^{2+}$ and $[Ru(tpy)(bpz)(OH_2)]^{2+}$ (tpy = 2,2′:6′,2″-terpyridine; bpm = 2,2′-bipyrimidine; bpz = 2,2′-bipyrazine) and a preliminary account of the mechanistic details by which water oxidation occurs. Oxidation is induced by proton-coupled electron transfer (PCET) and oxidative activation of $Ru^{II}{-}OH_2$ to $Ru^{IV}{=}O$, followed by further oxidation to $Ru^{V}{=}O$. Oxidative activation is followed by water attack on the oxo group to give a terminal peroxide in the key O−O bond-forming step,[14] which is reminiscent of the O−O bond-forming step proposed for the active manganese site in the OEC of PSII.[1,2,4]

Here we elaborate and extend the initial report and develop a detailed mechanism for single-site water oxidation. In this mechanism water oxidation occurs through a series of well-defined steps through discrete intermediates. We also show, in a preliminary way, the use of ligand variations to vary rates and, with it, the rate-limiting step and overall rate of catalysis.

Experimental Section

Materials and Methods. Distilled water was further purified by using a Milli-Q Ultrapure water purification system. Stock solutions of Ce^{IV} for kinetic and stoichiometric measurements were prepared from $(NH_4)_2Ce(NO_3)_6$ (99.99+%, Aldrich). Nitric acid (Trace Metal grade, 70%) was purchased from Fisher Scientific, and perchloric acid (70%, purified by redistillation, 99.999% trace metals basis) was purchased from Aldrich. 2,2′-Bipyrimidine (97%) and $RuCl_3{\cdot}H_2O$ were purchased from Aldrich and used as received. 2,6-Bis(1-methylbenzimidazol-2-yl)pyridine (Mebimpy) was prepared as reported for 2,6-bis(benzimidazol-2-yl)pyridine.[15] $[Ru(tpy)(bpm)(OH_2)](PF_6)_2$ was available from a previous study,[14] and [Ru(Mebimpy)(N−N)(Cl)](Cl) (N−N = bpy or bpm) was prepared by a modification of the procedure reported for $[Ru(tpy)(bpm)(Cl)](PF_6)$.[16] All other reagents were ACS grade and used without additional purification.

UV/vis spectra were recorded on an Agilent Technologies model 8453 diode-array spectrophotometer. Stopped-flow experiments

‡ University of North Carolina at Chapel Hill.
† Brookhaven National Laboratory.

(1) Renger, G. *Photosynth. Res.* **2007**, *92*, 407–425.
(2) Barber, J. *Biochem. Soc. Trans.* **2006**, *34*, 619–631.
(3) Renger, G.; Renger, T. *Photosynth. Res.* **2008**, *98*, 53–80.
(4) Meyer, T. J.; Huynh, M. H. V.; Thorp, H. H. *Angew. Chem., Int. Ed.* **2007**, *46*, 5284–5304.
(5) Gersten, S. W.; Samuels, G. J.; Meyer, T. J. *J. Am. Chem. Soc.* **1982**, *104*, 4029–4030.
(6) Gilbert, J. A.; Eggleston, D. S.; Murphy, W. R., Jr.; Geselowitz, D. A.; Gersten, S. W.; Hodgson, D. J.; Meyer, T. J. *J. Am. Chem. Soc.* **1985**, *107*, 3855–3864.
(7) Hurst, J. K. *Coord. Chem. Rev.* **2005**, *249*, 313–328.
(8) Binstead, R. A.; Chronister, C. W.; Ni, J.; Hartshorn, C. M.; Meyer, T. J. *J. Am. Chem. Soc.* **2000**, *122*, 8464–8473.
(9) Liu, F.; Concepcion, J. J.; Jurss, J. W.; Cardolaccia, T.; Templeton, J. L.; Meyer, T. J. *Inorg. Chem.* **2008**, *47*, 1727–1752.
(10) McDaniel, N. D.; Coughlin, F. J.; Tinker, L. L.; Bernhard, S. *J. Am. Chem. Soc.* **2008**, *130*, 210–217.
(11) Zong, R.; Thummel, R. P. *J. Am. Chem. Soc.* **2005**, *127*, 12802–12803.
(12) Deng, Z.; Tseng, H.-W.; Zong, R.; Wang, D.; Thummel, R. *Inorg. Chem.* **2008**, *47*, 1835–1848.
(13) Tseng, H.-W.; Zong, R.; Muckerman, J. T.; Thummel, R. *Inorg. Chem.* **2008**, *47*, 11763–11773.
(14) Concepcion, J. J.; Jurss, J. W.; Templeton, J. L.; Meyer, T. J. *J. Am. Chem. Soc.* **2008**, *130*, 16462–16463.
(15) Xu, X.; Xi, Z.; Chen, W.; Wang, D. *J. Coord. Chem.* **2007**, *60*, 2297–2308.

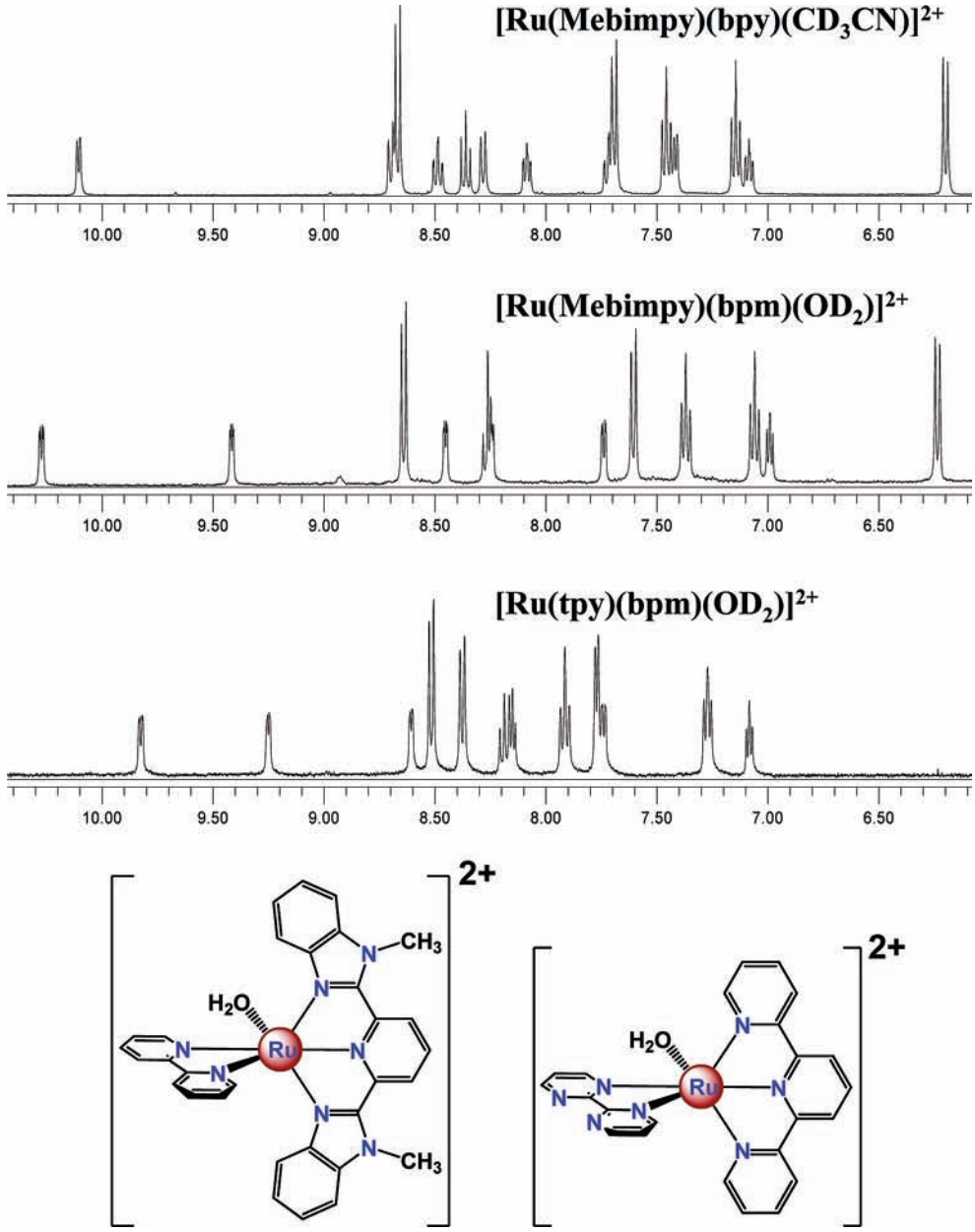

Figure 1. ^{1}H NMR spectra (400 MHz) for [Ru(N−N−N)(N−N)(OTf)](OTf) (N−N−N is tpy or Mebimpy) and structures of the complexes $[Ru(Mebimpy)(bpy)(OH_2)]^{2+}$ (left) and $[Ru(tpy)(bpm)(OH_2)]^{2+}$ (right). The solvents used in the NMR experiment, CD_3CN and D_2O, displace the triflate anion from the coordination sphere to give the corresponding solvento complexes, with the aqua complex shown in the figure.

were performed on a Hi-Tech SF-61 DX2 double-mixing stopped-flow system equipped with a diode array detector. The stopped volume was 100 μL, and the initial concentrations of reactants in the syringes (ruthenium complex and Ce^{4+}) were 5×10^{-5} and 5×10^{-4} M, respectively. Data were processed by use of the program SPECFIT/32 Global Analysis System (SPECTRUM Software Associates). Electrochemical measurements were performed on an EG&G Princeton Applied Research model 273A potentiostat/galvanostat. Voltammetric measurements were conducted with a planar EG&G PARC G0229 glassy carbon millielectrode, a platinum wire EG&G PARC K0266 counter electrode, and Ag/AgCl EG&G PARC K0265 reference electrode.

Oxygen Evolution Experiments. Oxygen measurements were performed with a calibrated O_2 electrode (YSI, Inc., model 550A). In a typical experiment, 30 equiv of Ce^{IV} was added to stirred solutions containing 2.9×10^{-3} M ruthenium complex in 1.0 M HNO_3. The airtight reaction cell was purged with argon prior to the addition of the Ce^{IV} until the digital readout had stabilized. O_2 evolution vs time was recorded, and the theoretical maximum was achieved ±3%.

Synthesis. 2,6-Bis(1-methylbenzimidazol-2-yl)pyridine (Mebimpy). This ligand was prepared by a modification of the procedure reported for 2,6-bis(benzimidazol-2-yl)pyridine.[15] A mixture of pyridine-2,6-dicarboxylic acid (3.35 g, 20 mmol) and *N*-methyl-1,2-phenylenediamine (5.38 g, 44 mmol) in 40 mL of 85% phosphoric acid was stirred at ca. 230 °C for 4 h. The dark green melt was poured into 1 L of vigorously stirred cold water. After the solution was cooled to room temperature, the blue precipitate was collected by filtration and then slurried into 300 mL of hot aqueous sodium carbonate solution (10%). The resulting solid was filtered off and recrystallized from methanol to give a white solid. Yield: 5.77 g, 85%. ^{1}H NMR ($CDCl_3$): δ 8.42 (d, 2H), 8.05 (t,

(16) Swavey, S.; Fang, Z.; Brewer, K. J. *Inorg. Chem.* **2002**, *41*, 2598–2607.

1H), 7.88 (dd, 2H), 7.46 (dd, 2H), 7.37 (qd, 4H), 4.25 (s, 6H, $2CH_3$). High-resolution MS (ESI, *m/z*): 362.1382 ($M + Na^+$).

[Ru(Mebimpy)Cl_3]. In a typical experiment $RuCl_3 \cdot 3H_2O$ (1.00 g, 3.83 mmol) and Mebimpy (1.30 g, 3.83 mmol) were mixed in 400 mL of ethanol, and the mixture was refluxed for 3 h. Upon the mixture cooling to room temperature, the brown solid was filtered, washed with ethanol until the ethanol came out clear, and finally washed with ether. Yield: 1.6 g, 76%. This compound was used without further purification.

[((Mebimpy)(Cl)Ru)$_2$$Cl_2$]. [Ru(Mebimpy)$Cl_3$] (500 mg,) was suspended in ethanol (40 mL) and the mixture degassed by bubbling argon trough it. Triethylamine (1.5 mL) was added and the mixture refluxed for 2 h and filtered hot. The purple solid obtained was washed with ethanol and ether to remove $[Ru(Mebimpy)_2]Cl_2$, which is soluble in ethanol. This impurity is the result of reduction of $[Ru(Mebimpy)_2]Cl_3$ that forms as a byproduct in the synthesis of [Ru(Mebimpy)Cl_3]. $[((Mebimpy)(Cl)Ru)_2Cl_2]$ is insoluble in most organic solvents and was used without further purification.

[Ru(Mebimpy)(bpy)(Cl)](Cl). $[((Mebimpy)(Cl)Ru)_2Cl_2]$ (300 mg, 0.29 mmol) and bpy (92 mg, 59 mmol) were suspended in 45 mL of 2:1 EtOH:H_2O, and the mixture was degassed by argon bubbling. The suspension was heated at reflux for 4 h, and 10 mL of 20% aqueous LiCl was added. After an additional 20 min, the mixture was filtered hot, and the filtrate was allowed to cool overnight. The brown microcrystalline solid formed was isolated by filtration and washed with water and ether. Yield: 329 mg, 85%. ^{1}H NMR (CD_3OD): δ 10.68 (d, 1H), 8.83 (d, 1H), 8.71 (d, 2H), 8.44−8.48 (td, 1H), 8.36 (d, 1H), 8.20−8.24 (t, 1H), 8.09−8.12 (td, 1H), 7.69 (d, 2H), 7.56−7.60 (td, 1H), 7.46 (d, 1H), 7.38−7.42 (t, 2H), 4.51 (s, 6H, $2CH_3$). High-resolution MS (ESI, *m/z*): 632.0903 (M^+).

[Ru(Mebimpy)(bpm)(Cl)](Cl). [Ru(Mebimpy)Cl_3] (700 mg, 1.28 mmol) and bpm (203 mg, 1.28 mmol) were suspended in 60 mL of 2:1 EtOH:H_2O, and the mixture was degassed by argon bubbling. Triethylamine (2.5 mL) was added with a syringe, and the suspension was heated at reflux for 4 h. Twenty milliliters of 20% aqueous LiCl was added, and the brown microcrystalline solid formed was isolated by filtration and washed with water and ether. Yield: 728 mg, 85%. ^{1}H NMR (CD_3CN): δ 10.89−10.91 (dd, 1H), 9.42−9.44 (dd, 1H), 8.58 (d, 3H), 8.13−8.18 (m, 2H), 7.70−7.72 (dd, 1H), 7.63 (d, 2H), 7.39−7.44 (td, 2H), 7.09−7.13 (t, 2H), 6.99−7.02 (t, 1H), 6.24 (d, 2H), 4.40 (s, 6H, $2CH_3$). High-resolution MS (ESI, *m/z*): 634.0808 (M^+).

[Ru(Mebimpy)(N−N)(OTf)](OTf). A mixture of [Ru(Mebimpy)-(N−N)(Cl)](Cl) (0.50 mmol) and AgOTf (1.05 mmol; OTf = triflate anion) in MeOH (40 mL) was stirred under argon at room temperature overnight. The silver chloride was removed by filtration using a bed of Celite, and the filtrate was taken to dryness by rotary evaporation. Diethyl ether was added, and the solid was filtered, washed with ether, and air-dried.

[Ru(Mebimpy)(bpy)(OTf)](OTf). ^{1}H NMR (CD_3CN, 400 MHz, as [Ru(Mebimpy)(bpy)(CD_3CN)]($OTf)_2$): δ 10.10 (d, 1H), 8.70 (d, 1H), 8.67 (d, 2H), 8.49 (td, 1H), 8.36 (t, 1H), 8.28 (d, 1H), 8.07−8.10 (m, 1H), 7.72 (td, 2H), 7.69 (d, 2H), 7.44−7.48 (m, 2H), 7.41 (d, 1H), 7.13−7.17 (m, 2H), 7.07−7.10 (m, 1H), 6.20 (d, 2H), 4.44 (s, 6H, $2CH_3$). Anal. Found (calcd) for $C_{33}H_{25}F_6N_7O_6RuS_2 \cdot 4H_2O$: C, 41.09 (40.99); N, 10.13 (10.14); H, 2.86 (3.44). High-resolution MS (ESI, *m/z*): 746.0735 (M^+).

[Ru(Mebimpy)(bpm)(OTf)](OTf). ^{1}H NMR (D_2O, 400 MHz, as [Ru(Mebimpy)(bpy)(D_2O)]($OTf)_2$): δ 10.27 (dd, 1H), 9.42 (d, 1H), 8.64 (d, 2H), 8.45 (dd, 1H), 8.26 (t, 2H), 8.24 (d, 1H), 7.74 (dd, 1H), 7.61 (d, 2H), 7.37 (t, 2H), 7.06 (t, 2H), 6.99 (t, 1H), 6.23 (d, 2H), 4.40 (s, 6H, $2CH_3$). Anal. Found (calcd) for $C_{31}H_{23}F_6N_9O_6RuS_2 \cdot 5H_2O$: C, 37.63 (37.73); N, 12.59 (12.77); H, 2.77 (3.37). High-resolution MS (ESI, *m/z*): 748.0640 (M^+).

[Ru(tpy)(bpm)(OH_2)]($PF6)_2$. ^{1}H NMR (D_2O, 400 MHz, as [Ru(tpy)(bpm)(D_2O)]($PF_6)_2$): δ 9.83 (d, 1H), 9.25 (d, 1H), 8.60 (dd, 1H), 8.52 (d, 2H), 8.38 (d, 2H), 8.19 (t, 1H), 8.15 (t, 1H), 7.91 (t, 2H), 7.77 (d, 2H), 7.73 (dd, 1H), 7.27 (t, 2H), 7.08 (t, 1H). Anal. Found (calcd) for $C_{23}H_{19}F_{12}N_7OP_2Ru \cdot H_2O$: C, 33.72 (33.75); N, 12.09 (11.98); H, 2.54 (2.59).

[Ru(Mebimpy)(N−N)(OH_2)]($OTf)_2$. The aquo complexes were generated in situ by dissolving the triflate complexes in water.

[Ru(Mebimpy)(bpy)(OH_2)]($OTf)_2$. UV−vis λ_{max}, nm (ϵ, M^{-1} cm^{-1}): in 0.1 M HNO_3, 487 (12600), 358 (40460), 343 (34700), 315 (27150), 290 (46300), 253 (sh, 32000), 245 (34700); in 0.01 M NaOH, 600 (sh, 3970), 518 (11620), 357 (39500), 342 (33050), 315 (24450), 292 (50500), 255 (sh, 26650), 241 (31770).

[Ru(Mebimpy)(bpm)(OH_2)]($OTf)_2$. UV−vis λ_{max}, nm (ϵ, M^{-1} cm^{-1}): in 0.1 M HNO_3, 526 (sh, 4120), 439 (9070), 359 (34180), 345 (28140), 316 (21700), 245 (37640); in 0.01 M NaOH, 572 (sh, 4840), 494 (8360), 358 (31400), 344 (25950), 315 (20350), 302 (18300), 262 (sh, 29650), 245 (33600).

[Ru(tpy)(bpm)(OH_2)]($PF_6)_2$. UV−vis λ_{max}, nm (ϵ, M^{-1} cm^{-1}): in 0.1 M HNO_3, 483 (7350), 428 (sh, 6220), 365 (7050), 332 (sh, 14720), 309 (29900), 270 (sh, 26500), 262 (27900), 240 (30900), 231 (sh, 29800); in 0.01 M NaOH, 521 (7390), 477 (sh, 6660), 384 (8130), 316 (27600), 274 (23300), 263 (sh, 25800), 237 (34900).

Theoretical Calculations. Theoretical calculations were carried out using Density Functional Theory (DFT) as implemented in Gaussian03, revision E.01.[17] Becke's three-parameter hybrid functional[18−21] with the LYP correlation functional[22] (B3LYP) was used with the Los Alamos effective core potential LanL2DZ basis set. The transition state was located with the Synchronous Transit-Guided Quasi-Newton (STQN) method, developed by Schlegel and co-workers.[23,24] The solvent was modeled by means of the Integral Equation Formalism Polarizable Continuum Model (IEF-PCM),[25−28] as implemented in Gaussian03.

The geometries of $[Ru^{III}(tpy)(bpm)(OOH)]^{2+}$, $[Ru^{IV}(tpy)(bpm)(\mu_2\text{-}O_2)]^{2+}$, $[Ru^{IV}(tpy)(bpm)(O-O)]^{2+}$, $[Ru^{V}(tpy)(bpm)(\mu_2\text{-}O_2)]^{2+}$, and $[Ru^{V}(tpy)(bpm)(O-O)]^{2+}$ were fully optimized. The multiplicities chosen were doublets for the Ru^{III} and Ru^{V} complexes and singlets for the Ru^{IV} complexes. Frequency calculations were performed on the optimized geometries to verify that they correspond to minima on each potential energy surface (PES). The final wave functions were tested for stability for each case, and when an instability was found other plausible electronic configurations were considered. The transition state for the reaction $[Ru^{IV}(tpy)(bpm)(\mu_2\text{-}O_2)]^{2+} \rightarrow [Ru^{IV}(tpy)(bpm)(\mu_1\text{-}O-O)]^{2+}$ in the singlet PES was found by using the QST3 option in the STQN method, as implemented in Gaussian03. The initial structure of the transition state was the geometry of highest energy from a relaxed coordinate scan of the relevant Ru−O distance in the equilibrium geometry for $[Ru^{IV}(tpy)(bpm)(\mu_2\text{-}O_2)]^{2+}$ to the equilibrium geometry in $[Ru^{IV}(tpy)(bpm)(\mu_1\text{-}O-O)]^{2+}$. A frequency calculation returned one negative frequency, and animation of the corresponding vibrations shows that it corresponds to the coordinate that interconverts the two forms.

(17) Frisch, M. J.; et al.; *Gaussian 03*, revision E.01; Gaussian Inc.: Wallingford, CT, 2004.
(18) Becke, A. D. *Phys. Rev., Ser. A* **1988**, *38*, 3098–3100.
(19) Becke, A. D. *Chem. Phys.* **1993**, *98*, 1372–1377.
(20) Becke, A. D. *J. Chem. Phys.* **1993**, *98*, 5648–5652.
(21) Stevens, P. J.; Devlin, F. J.; Chablowski, C. F.; Frisch, M. J. *J. Phys. Chem.* **1994**, *98*, 11623–11627.
(22) Lee, C.; Yang, W.; Parr, R. G. *Phys. Rev.* **1988**, *B37*, 785–789.
(23) Peng, C.; Schlegel, H. B. *Isr. J. Chem.* **1993**, *33*, 449.
(24) Peng, C.; Ayala, P. Y.; Schlegel, H. B.; Frisch, M. J. *J. Comput. Chem.* **1996**, *17*, 49.
(25) Tomasi, J.; Mennucci, B.; Cammi, R. *Chem. Rev.* **2005**, *105*, 2999–3093.
(26) Cancès, E.; Mennucci, B.; Tomasi, J. *J. Chem. Phys.* **1997**, *107*, 3032.
(27) Mennucci, B.; Cancès, E.; Tomasi, J. *J. Phys. Chem. B* **1997**, *101*, 10506.
(28) Cancès, E.; Mennucci, B. *J. Math. Chem.* **1998**, *23*, 309.

Single-point calculations were carried out on the optimized geometries with the solvent (water) modeled by means of the IEF-PCM.

Results

Synthesis. The three monomeric complexes employed in this study were synthesized in 60−80% overall yield by modification of known procedures for similar complexes (e.g., [Ru(tpy)(bpm)(Cl)](PF_6) and [Ru(tpy)(bpy)(OH_2)](ClO_4)$_2$).[16,29] Their proton NMR spectra display the expected pattern of resonances based on C_s symmetry (Figure 1). The σ plane is perpendicular to the tridentate ligand (tpy or Mebimpy). As a result, the protons from these ligands display a pattern of six resonances: one corresponding to the pyridine proton in the mirror plane and five corresponding to five pairs of equivalent protons from above and below the plane. All the protons in the bidentate ligands (bpy or bpm) are inequivalent, resulting in eight additional resonances for bpy and six additional resonances for bpm.

$[Ru(tpy)(bpm)(OH_2)]^{2+}$, $[Ru(Mebimpy)(bpy)(OH_2)]^{2+}$, and $[Ru(Mebimpy)(bpm)(OH_2)]^{2+}$ display metal-to-ligand charge-transfer absorptions in the visible at 483, 487, and 518 nm, respectively. These bands shift to lower energy upon deprotonation, $[Ru^{II}—OH_2]^{2+} + OH^- \rightarrow [Ru^{II}—OH]^+ + H_2O$ (494, 518, and 521 nm).

In an earlier communication the pH-dependence of the redox potentials for $Ru(tpy)(bpm)(OH_2)^{2+}$ (bpm = 2,2′-bipyrimidine) was reported.[14] It revealed the pattern of redox events summarized below at pH = 1 vs NHE:

(a) $Ru^{IV}=O^{2+}/Ru^{II}—OH_2^{2+}$, $E° = 1.16$ V; $[Ru^{III}—OH_2]^{3+}$ and $[Ru^{III}—OH]^{2+}$ are "missing" oxidation states due to disproportionation, $2[Ru—OH]^{2+} \rightarrow [Ru^{IV}=O]^{2+} + [Ru^{II}—OH_2]^{2+}$.

(b) $Ru^{V}=O^{3+}/Ru^{IV}=O^{2+}$, $E° = 1.65$ V at the onset of a catalytic water oxidation wave.

In Figure 2 is shown a cyclic voltammogram for $[Ru(Mebimpy)(bpy)(OH_2)]^{2+}$ (Mebimpy = 2,6-bis(1-methylbenzimidazol-2-yl)pyridine). In contrast to $[Ru(tpy)(bpm)(OH_2)]^{2+}$, separate waves are observed for the $Ru^{III}—OH^{2+}/Ru^{II}—OH_2^{2+}$ ($E° = 0.82$ V) and $Ru^{IV}=O^{2+}/Ru^{III}—OH^{2+}$ ($E° = 1.48$ V) couples. For this complex, both $Ru^{IV}=O^{2+}/Ru^{III}—OH^{2+}$ and $Ru^{V}=O^{3+}/Ru^{IV}=O^{2+}$ waves (1.62 V) occur at the onset of a catalytic water oxidation wave. The position of the last two waves was determined by square wave voltammetry.

Water Oxidation by $[Ru(tpy)(bpm)(OH_2)]^{2+}$. In Figure 3a are shown absorbance−time changes at 283 nm following addition of 3 equiv of Ce(IV) to $[Ru(tpy)(bpm)(OH_2)]^{2+}$ in 0.1 M $HClO_4$. Figure 3B shows absorption spectra at different times from the same experiment as well as the absorption spectrum of the dominant species at each stage of the time-resolved reaction in Figure 3a. These spectra were obtained in a photodiode array spectrophotometer with application of SPECFIT for spectral deconvolution. Absorption maxima and molar absorptivities are listed in Table 1.

The first step is rapid oxidation of $[Ru^{II}—OH_2]^{2+}$ to $[Ru^{IV}=O]^{2+}$, eqs 1 and 2. No evidence for $[Ru^{III}—OH]^{2+}$ as an intermediate was observed by stopped-flow kinetics under the conditions employed, showing that subsequent oxidation to $[Ru^{IV}=O]^{2+}$ is rapid on this time scale.

$$[Ru^{II}—OH_2]^{2+} + Ce^{4+} \xrightarrow{k_1} \{Ru^{III}—OH^{2+}\} + Ce^{3+} + H^+ \quad (1)$$

$$\{Ru^{III}—OH^{2+}\} + Ce^{4+} \xrightarrow{\text{rapid}} [Ru^{IV}=O]^{2+} + Ce^{3+} + H^+ \quad (2)$$

Following oxidation of $[Ru^{II}—OH_2]^{2+}$ to $[Ru^{IV}=O]^{2+}$, further oxidation to $[Ru^{V}=O]^{3+}$ (Table 1) occurs, followed by nucleophilic attack of water on $[Ru^{V}=O]^{3+}$, eq 3. This is the key O---O bond-forming step, which results in the putative intermediate, $[Ru^{III}—OOH]^{2+}$. It was characterized by redox titration. In this experiment Fe_{aq}^{2+}, as $(NH_4)_2Fe(SO_4)_2$, was added incrementally to solutions of $[Ru(tpy)(bpm)(OOH)]^{2+}$ generated by addition of 3 equiv of Ce(IV) with spectrophotometric monitoring. Quantitative conversion to the characteristic spectrum of $[Ru(tpy)(bpm)(OH_2)]^{2+}$ was observed following addition of 3 equiv of Fe_{aq}^{2+}, eq 4.

$$Ru^{V}=O^{3+} + H_2O \xrightarrow{k_{O-O}} Ru^{III}—O_2H^{2+} + H^+ \quad (3)$$

$$Ru^{III}—O_2H^{2+} + 3Fe^{2+} + 3H^+ \rightarrow Ru^{II}—OH_2^{2+} + 3Fe^{3+} + H_2O \quad (4)$$

$[Ru^{III}—OOH]^{2+}$ is unstable over extended periods (hours) decomposing quantitatively to $[Ru^{II}—OH_2]^{2+}$. This conversion has not yet been studied in detail but may involve initial disproportionation into $[Ru^{II}(H_2O_2)]^{2+}$ and $[Ru^{IV}(OO)]^{2+}$.

Upon addition of 30 equiv of Ce(IV) to $[Ru—OH_2]^{2+}$ under catalytic conditions, the dominant species at the catalytic steady state is an intermediate presumably formed by further one-electron oxidation of $[Ru^{III}—OOH]^{2+}$ to $[Ru^{IV}(OO)]^{2+}$ (Figure 4 and Table 1).

The kinetics of Ce(IV) consumption under catalytic conditions are zeroth-order in Ce(IV), as can be seen in Figure 5a. For a zeroth-order reaction, the rate of appearance of product is $dC/dt = k$, with C the concentration at time t and k the zeroth-order rate constant in M s^{-1}. Integration gives $C - C_0 = kt$. Since $C = A/\varepsilon b$ (where A is absorbance, ε is molar absorptivity, and b is the path length of the cell), $A/\varepsilon b - A_0/\varepsilon b = kt$. Zeroth-order rate constants were obtained from plots of $A/\varepsilon b$ versus t.

A plot of zeroth-order rate constant determined in this manner versus the initial concentration of $[Ru^{II}—OH_2]^{2+}$ over the range 3.1×10^{-5}−1.2×10^{-4} M in $[Ru^{II}—OH_2]^{2+}$ is shown in Figure 5b. The same behavior, independent of anion with comparable rate constants, was observed in HNO_3, HOTf, or $HClO_4$, ruling out aquation of an anated intermediate followed by oxidation. The appearance of zeroth-order kinetics is consistent with rate-limiting decomposition of a second intermediate formed by oxidation of $[Ru^{III}—OOH]^{2+}$. The second intermediate decomposes with $k(25\ °C) = 7.5 \times 10^{-4}$ s^{-1} in 0.1 M HNO_3 and appears to be $[Ru^{IV}(OO)]^{2+}$ in which the peroxide is bound in an η^2 bidentate fashion, based on literature precedence and DFT calculations (see below).

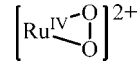

In 1.0 M HNO_3, the rate-limiting step in the catalytic cycle changes to oxidation of $[Ru^{IV}(OO)]^{2+}$. Under these conditions the rate law becomes first order in [Ce(IV)] and first order in

(29) Takeuchi, K. J.; Thompson, M. S.; Pipes, D. W.; Meyer, T. J. *Inorg. Chem.* **1984**, *23*, 1845–1851.

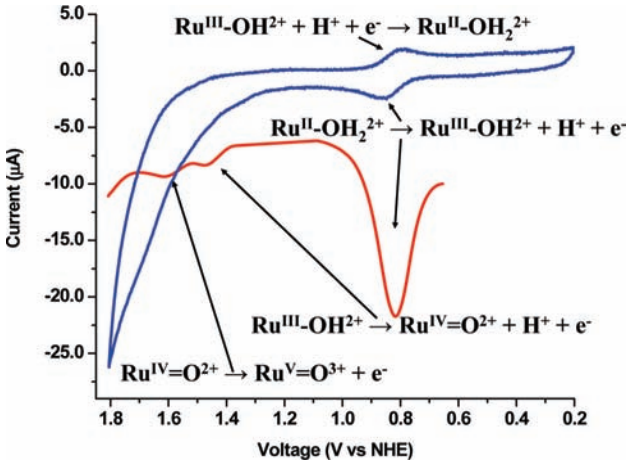

Figure 2. (Blue) Cyclic voltammogram for $[Ru(Mebimpy)(bpy)(OH_2)]^{2+}$ in 0.1 M HNO_3. Working electrode, glassy carbon electrode; scan rate, 10 mV/s. (Red) Square wave voltammogram for $[Ru(Mebimpy)(bpy)(OH_2)]^{2+}$ in 0.1 M HNO_3 (step, 4 mV; amplitude, 10 mV; frequency, 15 s^{-1}).

$[Ru^{IV}(OO)^{2+}]$, as observed by following Ce(IV) consumption at 360 nm (Figure 6a,b), eq 5.

$$\text{rate} = \frac{d[Ce(IV)]}{dt} = k[Ce(IV)][Ru^{IV}(OO)^{2+}] \qquad (5)$$

At the catalytic steady state, the concentration of $[Ru^{IV}(OO)]^{2+}$ is constant, and the rate law becomes pseudo-first-order in [Ce(IV)], with $k_{obs} = k[Ru^{IV}(OO)^{2+}]$, eq 6.

$$\frac{d[Ce(IV)]}{dt} = k_{obs}[Ce(IV)] \qquad (6)$$

From the plot of k_{obs} vs $[Ru^{IV}(OO)^{2+}]$ (taken to be the initial concentration of $[Ru(tpy)(bpm)(OH_2)]^{2+}$) in Figure 6b, k(25 °C, 1 M HNO_3) = 13 M^{-1} s^{-1}. Mechanistic studies on water oxidation by the blue dimer also show a change in rate-limiting step in the catalytic mechanism between 0.1 and 1.0 M HNO_3. This effect has been attributed to the increase in $E^{o\prime}$(Ce(VI/III)) (from 1.50 V in 0.1 M HNO_3 to 1.61 V in 1.0 M HNO_3), which enhances the rate of oxidation of $[Ru^{IV}(OO)]^{2+}$ to $[Ru^{V}(OO)]^{2+}$.[9]

An additional complication appears in the kinetics data at higher concentrations of $[Ru(tpy)(bpm)(OH_2)]^{2+}$, with evidence for a pathway that is second order in complex (Figure 6c). We have observed this behavior with other monomeric catalysts as well, and it will be discussed in detail in a separate manuscript.

Oxygen Evolution. Measurements of O_2 production under catalytic conditions with 30 equiv of Ce(IV) were conducted with an oxygen electrode. The results obtained are consistent with stoichiometric oxygen production based on added Ce(IV), eq 7. Oxygen monitoring with an oxygen electrode in three separate experiments gave 100(±3)% of the expected O_2 after 7.5 turnovers upon addition of 30 equiv of Ce^{IV} to solutions containing 2.9×10^{-3} M ruthenium complex in 1.0 M HNO_3.

$$4Ce^{4+} + 2H_2O \xrightarrow{\text{catalyst}} 4Ce^{3+} + O_2 + 4H^+ \qquad (7)$$

Mechanism. The observations described above are consistent with the mechanism in Scheme 1.

Rate Constants. k_1: k_1 was obtained by stopped-flow mixing of 2 equiv of Ce(IV) with $[Ru^{II}—OH_2]^{2+}$ and observing absorbance−time changes at 485 nm. For this complex, $[Ru^{III}—OH]^{2+}$ is a missing oxidation state because it is unstable with respect to disproportionation and does not appear as a discernible intermediate.

The rate law under these conditions is given by eq 8, which includes a stoichiometric factor of 2,

$$-\frac{d[Ru^{II}]}{dt} = k_1[Ru^{II}][Ce^{4+}] = 2k_1[Ru^{II}]^2 = k_{obs}[Ru^{II}]^2 \qquad (8)$$

with $k_{obs} = 2k_1$. The integrated form of this expression, eq 9, was used to determine k_{obs}. In eq 9, A, A_0, and A_∞ are absorbances at time t, 0, and infinity, respectively. The initial concentration of complex is $[Ru^{II}]_0$.

$$\frac{(A_0 - A_\infty)}{[Ru^{II}]_0(A - A_\infty)} = k_{obs}t + \frac{1}{[Ru^{II}]_0} \qquad (9)$$

k_2: Oxidation of $[Ru^{IV}=O]^{2+}$ to $[Ru^{V}=O]^{3+}$ was followed spectrophotometrically at 283 nm following addition of 1 equiv of Ce(IV) to $[Ru^{IV}=O]^{2+}$. The reaction follows second-order equal concentration kinetics, eq 9, with $k_{obs} = k_2$.

$$Ru^{IV}=O^{2+} + Ce^{4+} \xrightarrow{k_2} Ru^{v} = O^{3+} + Ce^{3+} \qquad (10)$$

k_{O-O}: Once formed, $[Ru^{V}=O]^{3+}$ undergoes a further reaction with first-order kinetics, eq 11, by a process separated in time from oxidation of $[Ru^{IV}=O]^{2+}$ to $[Ru^{V}=O]^{3+}$.The rate constant was obtained from absorbance−time measurements by application of the integrated expression in eq 12.

$$-\frac{d[Ru^{III}—OOH^{2+}]}{dt} = k_{O-O}[Ru^{III}—OOH^{2+}] \qquad (11)$$

$$\ln\left(\frac{A - A_0}{A_\infty - A_0}\right) = k_{O-O}t \qquad (12)$$

k_3: The rate constant for the oxidation of $[Ru^{III}—OOH]^{2+}$ to $[Ru^{IV}(OO)]^{2+}$, eq 13, could not be determined from stopped-flow kinetic measurements. Once formed, $[Ru^{III}—OOH]^{2+}$ undergoes rapid oxidation to $[Ru^{IV}(OO)]^{2+}$.

$$Ru^{III}—OOH^{2+} + Ce^{4+} \xrightarrow{k_4} Ru^{IV}—OO^{2+} + Ce^{3+} + H^+ \qquad (13)$$

k_4: Under catalytic conditions in 0.1 M HNO_3, $[Ru^{IV}(OO)]^{2+}$ builds up,and its first-order decomposition is rate limiting, with k_4(25 °C) = 7.5×10^{-4} s^{-1}, as described in the previous section.

k_5: In 1.0 M HNO_3, Ce(IV) oxidation of $[Ru^{IV}(OO)]^{2+}$ to $[Ru^{V}(OO)]^{3+}$ is rate limiting and, as noted above, occurs with k_5(25 °C,1.0 M HNO_3) = 13 M^{-1} s^{-1}.

The complete mechanism is shown in Scheme 1, including the competition between first-order decomposition of $[Ru^{IV}(OO)]^{2+}$ and its further oxidation by Ce(IV). Rate constants labeled in Scheme 1 are listed in Table 2.

DFT Evaluation of Structures, Characterization, and Reactivities of Key Intermediates. $[Ru^{III}—OOH]^{2+}$. There is precedence for terminal peroxides in the literature, and a number of these complexes for cobalt, rhodium, iridium, palladium, and platinum have been crystallographically characterized.[30−38] The formation of $[Ru^{III}—OOH]^{2+}$ by reaction of $[Ru^{V}=O]^{3+}$ with water is reminiscent of the O−O bond formation step proposed for the OEC of PSII by nucleophilic attack of water on the

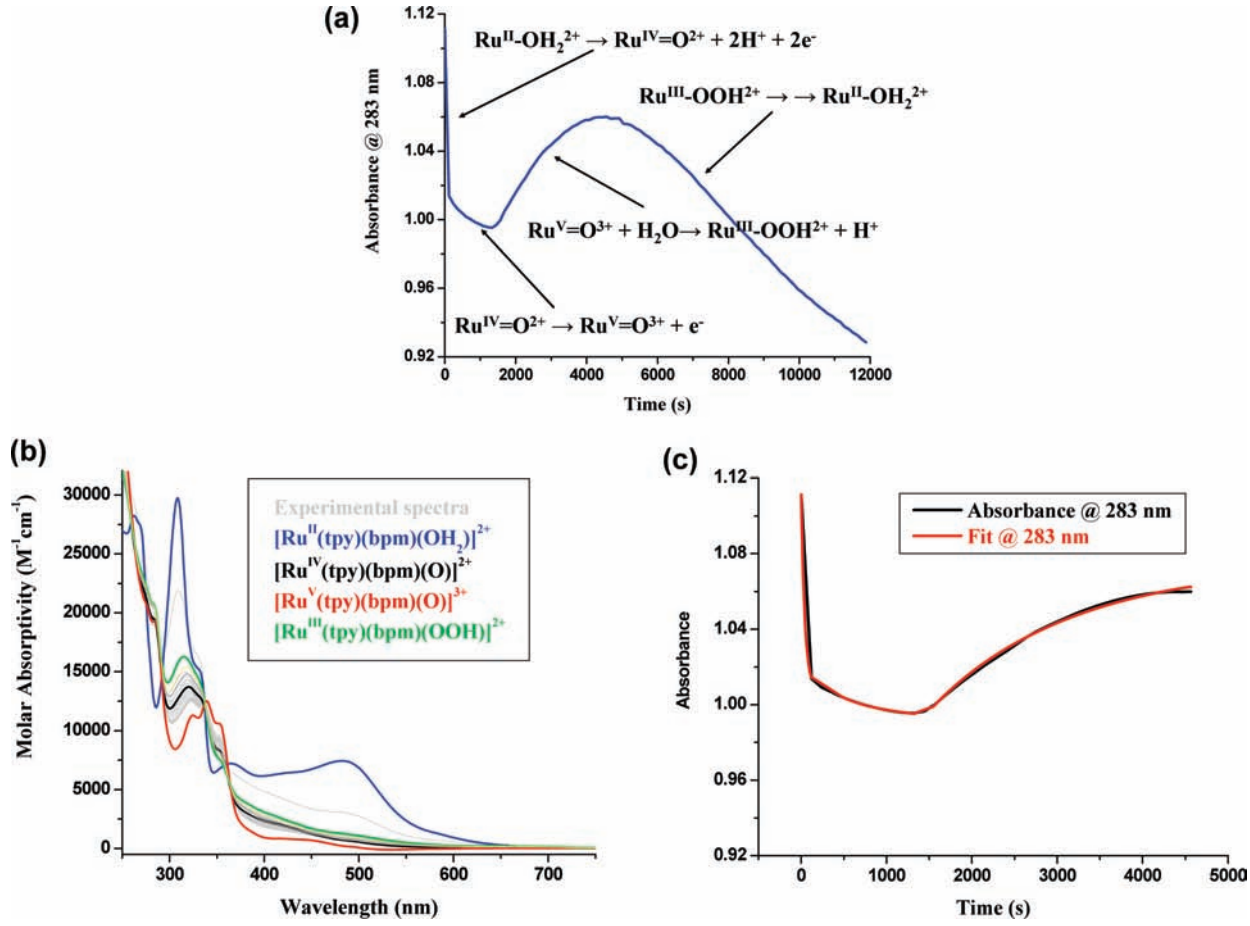

Figure 3. (a) Absorbance−time changes at 283 nm following addition of 3 equiv of Ce(IV) to $[Ru(tpy)(bpm)(OH_2)]^{2+}$ in 0.1 M $HClO_4$. The absorbance changes at this wavelength provide the clearest evidence for the reaction sequence since $\Delta A < 0$ for $Ru^{IV}{=}O \rightarrow Ru^{V}{=}O$; $\Delta A > 0$ for $Ru^{V}{=}O \rightarrow Ru^{III}{-}OOH$; and $\Delta A < 0$ for $Ru^{III}{-}OOH \rightarrow \rightarrow Ru^{II}{-}OH_2$. (b) Absorption spectra at different times from the same experiment (0−4500 s range) and absorption spectra of the dominant species at each stage of the reaction from the same experiment as derived from SPECFIT. (c) Absorbance−time changes at 283 nm and corresponding fit.

Table 1. Visible and Ultraviolet Spectrophotometric Parameters for Intermediates in the Water Oxidation Catalytic Cycle for $[Ru(tpy)(bpm)(OH_2)]^{2+}$ in 0.1 M $HClO_4$

complex	λ_{max}, nm (ϵ, M^{-1} m^{-1})
$[Ru^{II}(tpy)(bpm)(OH_2)]^{2+}$	483 (7350), 428 (sh, 6220), 365 (7050), 332 (sh, 14720), 309 (29900), 270 (sh, 26500), 262 (27900), 240 (30900), 231 (sh, 29800)
$[Ru^{IV}(tpy)(bpm)(O)]^{2+}$	668 (100), 420 (sh, 1940), 354 (sh, 8220), 334 (sh, 12600), 320 (13700), 284 (sh, 19400)
$[Ru^{V}(tpy)(bpm)(O)]^{3+}$	657 (50), 446 (720), 422 (sh, 820), 353 (10600), 339 (12500), 325 (11300), 285 (19300)
$[Ru^{III}(tpy)(bpm)(OOH)]^{2+}$	670 (sh, 180), 497 (sh, 1130), 354 (sh, 7500), 332 (sh, 14200), 315 (16300), 283 (sh, 20800)
$[Ru^{IV}(tpy)(bpm)(OO)]^{2+}$	665 (90), 418 (sh, 1890), 353 (sh, 8770), 335 (sh, 12390), 322 (13230), 283 (sh, 19660)

appended $Mn^{IV}{=}O$.[1] "O-atom transfer" is a common and well-defined reaction for $Ru^{IV}{=}O$ complexes such as $[Ru^{IV}(bpy)_2(py)(O)]^{2+}$ with sulfides, phosphines, and olefins.[39]

Characterization of $[Ru^{III}{-}OOH]^{2+}$. The proposed $[Ru^{III}{-}OOH]^{2+}$ structure is a minimum in the potential energy surface for this complex, as demonstrated by frequency calculations. The calculated ground state is a doublet with the spin density localized mostly at Ru, as anticipated for a $d\pi^5$ Ru(III) polypyridyl complex.

$[Ru^{III}(tpy)(bpm)(OOH)]^{2+}$ has been characterized by redox titration with Fe(II), eq 4. Its analogues, $[Ru^{III}(Mebimpy)(bpy)(OOH)]^{2+}$ and $[Ru^{III}(Mebimpy)(bpm)(OOH)]^{2+}$, are longer-

(30) Schaefer, W. P.; Huie, B. T.; Kurilla, M. G.; Ealick, S. E. *Inorg. Chem.* **1980**, *19*, 340–344.
(31) Guzei, I. A.; Bakac, A. *Inorg. Chem.* **2001**, *40*, 2390–2393.
(32) Takahashi, Y.; Hashimoto, M.; Hikichi, S.; Akita, M.; Moro-Oka, Y. *Angew. Chem., Int. Ed.* **1999**, *38*, 3074–3077.
(33) Carmona, D.; Lamata, M. P.; Ferrer, J.; Modrego, J.; Perales, M.; Lahoz, F. J.; Atencio, R.; Oro, L. A. *J. Chem. Soc., Chem. Commun.* **1994**, 575–576.
(34) Ahijado, M.; Braun, T.; Noveski, D.; Kocher, N.; Neumann, B.; Stalke, D.; Stammler, H.-G. *Angew. Chem., Int. Ed.* **2005**, *44*, 6947–6951.
(35) Miyaji, T.; Kujime, M.; Hikichi, S.; Moro-oka, Y.; Akita, M. *Inorg. Chem.* **2002**, *41*, 5286–5295.
(36) Denney, M. C.; Smythe, N. A.; Cetto, K. L.; Kemp, R. A.; Goldberg, K. I. *J. Am. Chem. Soc.* **2006**, *128*, 2508–2509.
(37) Wick, D. D.; Goldberg, K. I. *J. Am. Chem. Soc.* **1999**, *121*, 11900–11901.
(38) Rostovtsev, V. V.; Henling, L. M.; Labinger, J. A.; Bercaw, J. E. *Inorg. Chem.* **2002**, *41*, 3608–3619.

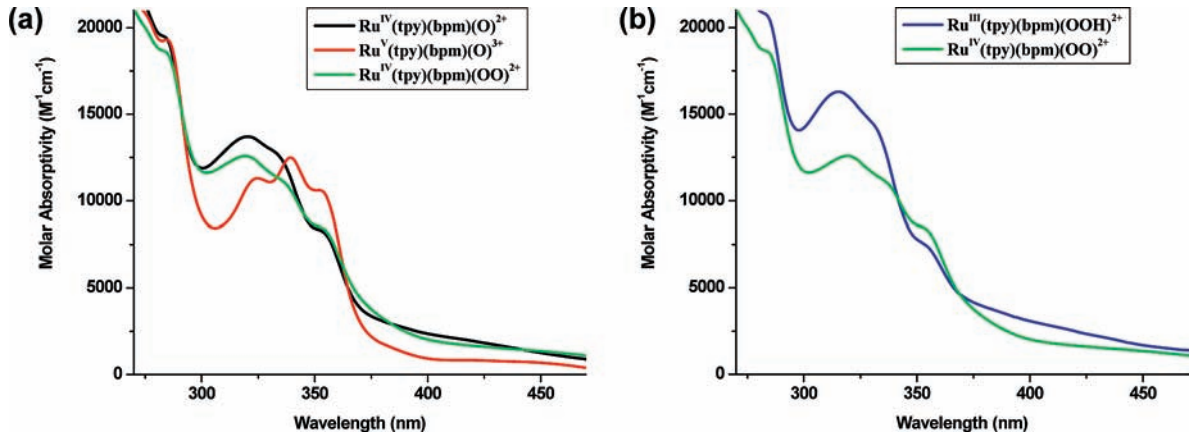

Figure 4. (a) Absorption spectrum of the dominant species at the catalytic steady state in 0.1 M $HClO_4$, $[Ru^{IV}(OO)]^{2+}$ (see text), following addition of 30 equiv of Ce(IV) to 5.1×10^{-5} M $[Ru(tpy)(bpm)(OH_2)]^{2+}$ ($[Ru{-}OH_2]^{2+}$) near the end of the catalytic cycle. For comparison, spectra of $[Ru^{IV}(O)]^{2+}$ (by addition of 2 equiv of Ce^{4+}) and $[Ru^{V}(O)]^{3+}$ (obtained by spectral deconvolution, see Figure 3) are also shown. (b) Absorption spectra of $[Ru^{IV}(OO)]^{2+}$ (as in panel a) and $[Ru^{III}{-}OOH]^{2+}$ (as in Figure 3b) in 0.1 M $HClO_4$.

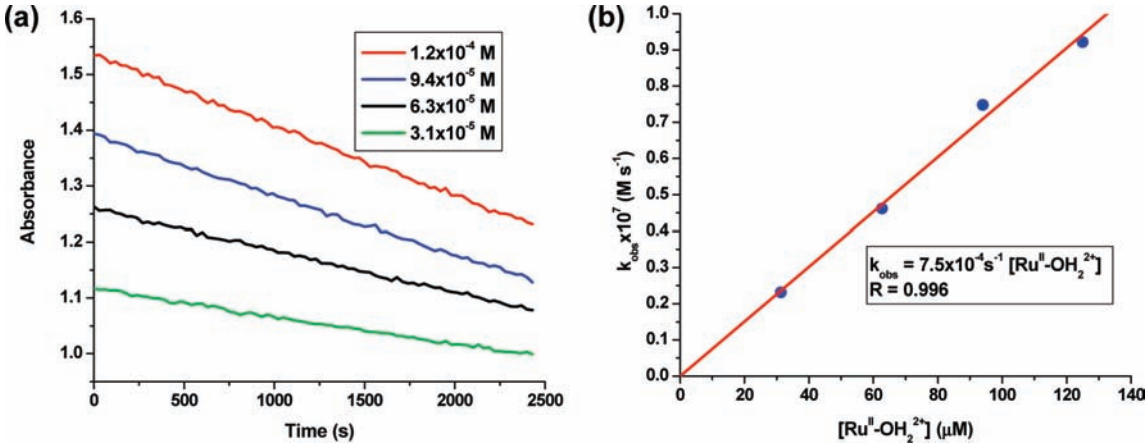

Figure 5. (a) Ce(IV) monitoring at 360 nm after addition of 30 equiv of Ce(IV) to solutions of $[Ru(tpy)(bpm)(OH_2)]^{2+}$ at various concentrations of complex in 0.1 M HNO_3. (b) Plot of k_{obs} (determined from the data in panel a) vs $[Ru(tpy)(bpm)(OH_2)^{2+}]$. As can be seen from the plot, the kinetics for Ce(IV) disappearance are first order in $[Ru(tpy)(bpm)(OH_2)^{2+}]$, with a first-order rate constant of 7.5×10^{-4} s^{-1}.

lived and more amenable to spectral characterization. Ru(III) and higher oxidation state Mebimpy complexes display characteristic ligand-to-metal charge-transfer (LMCT) bands in the low-energy visible, providing a convenient signature for monitoring and characterization.

Figure 7a shows absorbance−time changes following addition of 3 equiv of Ce(IV) to $[Ru^{II}(Mebimpy)(bpm)(OH_2)]^{2+}$ (5.1×10^{-5} M) in 0.1 M HNO_3 at 25 ± 2 °C. Three processes are clearly discernible in the time-resolved spectra: (i) the final stage in oxidation of $[Ru^{III}{-}OH]^{2+}$ to $[Ru^{IV}{=}O]^{2+}$, (ii) oxidation of $[Ru^{IV}{=}O]^{2+}$ to $[Ru^{V}{=}O]^{3+}$, and (iii) conversion of the latter to the analogue of $[Ru^{III}{-}OOH]^{2+}$ with $k_{O-O} = 1.4 \times 10^{-3}$ s^{-1}. Oxidation of $[Ru^{II}{-}OH_2]^{2+}$ to $[Ru^{III}{-}OH]^{2+}$ occurs in less than 0.4 s under these conditions, as determined by stopped-flow spectrophotometry, and is not observed as an intermediate on the time scale of the experiment in Figure 7a.

Figure 7b illustrates the absorption spectrum at the end of the reaction, when the absorbance at 637 nm reaches a maximum (~2700 s). Figure 8a illustrates the absorption spectra of $[Ru^{III}(Mebimpy)(bpy)(OH)]^{2+}$, $[Ru^{III}(Mebimpy)(bpy)(OOH)]^{2+}$, and $[Ru^{III}(Mebimpy)(bpm)(OOH)]^{2+}$ in 0.1 M HNO_3, the latter generated *in situ* with addition of 3 equiv of Ce(IV). They all display a LMCT band (see below) in the low-energy visible ($\lambda_{max} = 629$, 638, and 638 nm, respectively) and similar ligand-centered $\pi\pi^*$ bands between 300 and 400 nm. The similarity in spectra between the $[Ru^{III}{-}OH]^{2+}$ complex and intermediates supports the identification of the latter as $[Ru^{III}(Mebimpy)(bpy)(OOH)]^{2+}$ and $[Ru^{III}(Mebimpy)(bpm)(OOH)]^{2+}$. Figure 8b shows the calculated absorption spectrum for $[Ru^{III}(Mebimpy)(bpy)(OOH)]^{2+}$ in water (TD-DFT, IEFPCM) and illustrates the molecular orbitals associated with the low-energy visible transition. The calculated spectrum is in reasonable agreement with the experimental spectrum and the orbitals involved with a LMCT transition.

Additional evidence for $Ru^{III}{-}OOH^{2+}$ comes from cyclic voltammetry. A solution 1.0 mM in $[Ru^{III}(Mebimpy)(bpm)$-

(39) Meyer, T. J.; Huynh, M. H. V. *Inorg. Chem.* **2003**, *42*, 8140–8160.
(40) Navarro Clemente, M. E.; Juarez Saavedra, P.; Cervantes Vasquez, M.; Paz-Sandoval, M. A.; Arif, A. M.; Ernst, R. D. *Organometallics* **2002**, *21*, 592–605.
(41) Shen, J.; Stevens, E. D.; Nolan, S. P. *Organometallics* **1998**, *17*, 3875–3882.
(42) Jia, G.; Ng, W. S.; Chu, H. S.; Wong, W.-T.; Yu, N.-T.; Williams, I. D. *Organometallics* **1999**, *18*, 3597–3602.
(43) Lindner, E.; Haustein, M.; Fawzi, R.; Steimann, M.; Wegner, P. *Organometallics* **1994**, *13*, 5021–5029.
(44) de los Rios, I.; Tenorio, M. J.; Padilla, J.; Puerta, M. C.; Valerga, P. *J. Chem. Soc., Dalton Trans.* **1996**, *3*, 377–381.

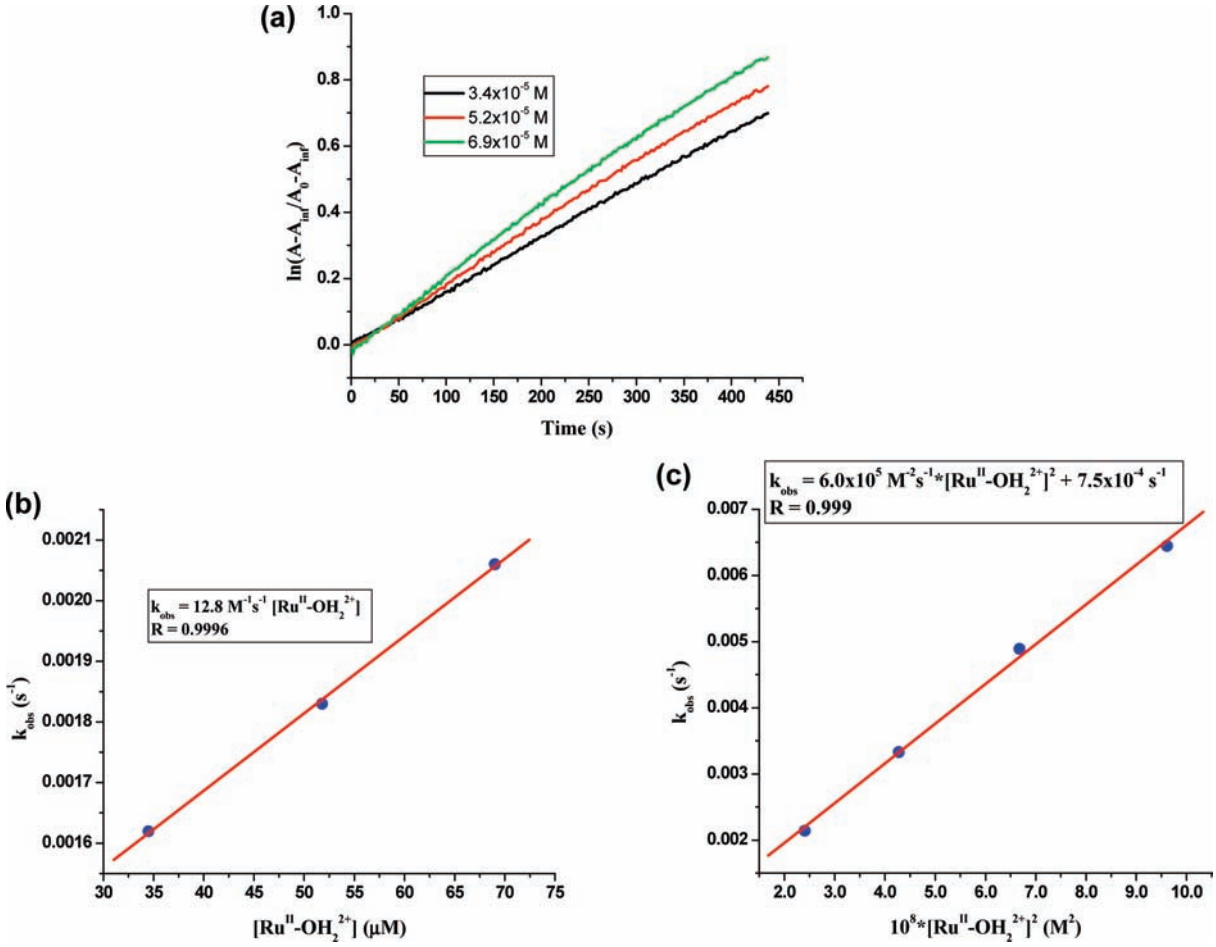

Figure 6. (a) Ce(IV) monitoring at 360 nm after addition of 30 equiv of Ce(IV) to $[Ru(tpy)(bpm)(OH_2)]^{2+}$ at various concentrations in 1.0 M HNO_3. (b) Plot of k_{obs} (determined from the data shown in Figure 5a) vs initial $[Ru(tpy)(bpm)(OH_2)^{2+}]$ ($[Ru^{II}—OH_2^{2+}] < 55\ \mu M$). From these data, the disappearance of Ce(IV) is first order in Ce(IV) and first order in $[Ru(tpy)(bpm)(OH_2)^{2+}]$, with $k = 13\ M^{-1}\ s^{-1}$. (c) Plot of k_{obs} vs the square of the initial $[Ru(tpy)(bpm)(OH_2)^{2+}]$ ($[Ru^{II}—OH_2^{2+}] > 155\ \mu M$). From these data, disappearance of Ce(IV) is first order in Ce(IV) and second order in $[Ru(tpy)(bpm)(OH_2)^{2+}]$, with $k = 6.0 \times 10^5\ M^{-2}\ s^{-1}$.

Scheme 1. Proposed Single-Site Water Oxidation Mechanism

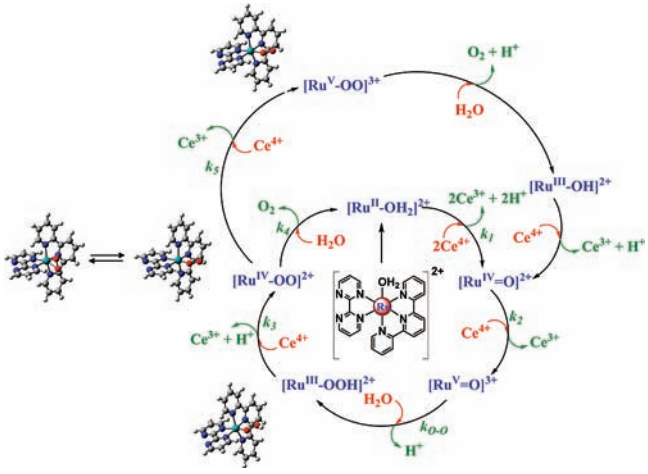

$(OOH)]^{2+}$ was generated in 0.1 M HNO_3 at 25 ± 2 °C by adding 3 equiv of Ce(IV) to $[Ru^{II}(Mebimpy)(bpm)(OH_2)]^{2+}$. Aliquots were taken over time and monitored spectrophotometrically to ensure maximum conversion to $[Ru^{III}(Mebimpy)(bpm)(OOH)]^{2+}$. Figure 9 shows cyclic voltammograms of the resulting solution as well as square wave voltammograms for both $[Ru^{III}(Mebimpy)(bpm)(OOH)]^{2+}$ and $[Ru^{II}(Mebimpy)(bpm)(OH_2)]^{2+}$. Reversible one-electron waves appear at 0.84, 0.97, and 1.40 V. By analogy with $[Ru^{II}(Mebimpy)(bpm)(OH_2)]^{2+}$, the first and third waves can be assigned to $Ru^{III}—OOH^{2+}/Ru^{II}—O_2H_2^{2+}$ and $Ru^{IV}—OO^{2+}/Ru^{III}—OOH^{2+}$ couples. The second wave at 0.97 V can be easily assigned to $Ru^{III}—OH^{2+}/Ru^{II}—OH_2^{2+}$ by comparison of the two square wave voltammograms. They occur at lower potentials by ~130 and ~270 mV, respectively, compared to the corresponding $Ru^{III}—OH^{2+}/Ru^{II}—OH_2^{2+}$ and $Ru^{IV}=O^{2+}/Ru^{III}—OH^{2+}$ couples. The decrease points to greater stabilization of Ru(III) by —OOH compared to —OH and of Ru(IV) with peroxide bound in an η^2 bidentate fashion compared to Ru=O.

Corroboration for nucleophilic attack of water on $[Ru^{V}=O]^{3+}$ comes from analysis of the evolved oxygen. We have performed ^{18}O-labeling experiments in collaboration with Prof. Antoni Llobet in 0.1 M triflic acid, and the results support the single-site mechanism: the oxygen originates from nucleophilic attack of water on $[Ru^{V}=O]^{3+}$. These results will be published in a separate manuscript.

$[Ru^{IV}(OO)]^{2+}$. There is precedence for Ru(IV) peroxo complexes in the literature, and a number of them have been crystallographically characterized.[40−44] They are all seven-coordinate with η^2 bidentate peroxo coordination. DFT calculations predict a singlet ground state for this geometry in $[Ru(tpy)(bpm)(O_2)]^{2+}$. There is also a six-coordinate isomer with

Table 2. Rate Constants in Scheme 1 at 25 ± 2 °C in 0.1 M HNO_3 (k_1-k_4) and 1.0 M HNO_3 (k_5) for Ce(IV)-Catalyzed Water Oxidation by $[Ru(tpy)(bpm)(OH_2)]^{2+}$

rate constant	value	reaction
k_1	$2.4 \times 10^2\ M^{-1}\ s^{-1}$	$Ru^{II}-OH_2^{2+} \xrightarrow{-2e^-,\ -2H^+} Ru^{IV}=O^{2+}$
k_2	$5.0\ M^{-1}\ s^{-1}$	$Ru^{IV}=O^{2+} \xrightarrow{-e^-} Ru^{V}=O^{3+}$
k_{O-O}	$9.6 \times 10^{-3}\ s^{-1}$	$Ru^{IV}=O^{3+} + H_2O \xrightarrow{-H^+} Ru^{III}-OOH^{2+}$
k_3	–	$Ru^{III}-OOH^{2+} \xrightarrow{-e^-,\ -H^+} Ru^{IV}(OO)^{2+}$
k_4	$7.5 \times 10^{-4}\ s^{-1}$	$Ru^{IV}(OO)^{2+} \xrightarrow{+H_2O} Ru^{II}-OH_2^{2+} + O_2$
k_5	$13\ M^{-1}\ s^{-1}$	$Ru^{IV}(OO)^{2+} \xrightarrow{-e^-} Ru^{V}(OO)^{3+}$

an open, terminal peroxide, as illustrated in Figure 10. In the open structure, the closed-shell singlet, the triplet, and the broken-symmetry singlet states are close in energy. The triplet is lower by 5.0 kcal/mol with respect to the closed-shell singlet (gas phase). The broken-symmetry singlet lies 1.6 kcal/mol above the triplet. These open-shell configurations might play a role in the oxygen evolution step (see below).

The seven-coordinate bidentate peroxide is 1.6 kcal/mol more stable than the closed-shell singlet of the terminal peroxide in the gas phase and 3.3 kcal/mol more stable in water based on a polarizable continuum model for the solvent (IEFPCM) (Figure 10). The transition state for interconversion between these two isomers is 17.5 kcal/mol above the bidentate form (solvated phase, Figure 10).

Preliminary Raman data have been obtained for $[Ru^{IV}(Mebimpy)(bpy)(\eta^2\text{-}OO)]^{2+}$ with 442 nm excitation on a Horiba Jobin Yvon LabRam Aramis Microscope spectrometer. In these spectra, in addition to characteristic Raman-allowed ligand bands, a band appears at 1015 cm^{-1}, consistent with the O−O stretch of the peroxide (Figure 11). This band energy is in good agreement with the value calculated by DFT (1015 cm^{-1}). We have not obtained unequivocal evidence for peroxide stretches in the other peroxidic intermediates. They are expected to be of low intensity and difficult to observe since the DFT analysis predicts very low Raman activities.

$[Ru^{V}(OO)]^{3+}$. Kinetic studies in 1.0 M HNO_3 reveal an additional pathway in the mechanism. Under these conditions the rate-limiting step is first order in Ce^{4+} and first order in complex, indicative of further oxidation of $[Ru^{IV}(OO)]^{2+}$, presumably to give $[Ru^{V}(OO)]^{3+}$, followed by rapid O_2 evolution, eqs 14 and 15.

$$Ru^{IV}(OO)^{2+} + Ce^{4+} \xrightarrow{k_5} Ru^{V}(OO)^{3+} + Ce^{3+} \qquad (14)$$

$$Ru^{V}-OO^{3+} + H_2O \xrightarrow{\text{rapid}} Ru^{III}-OH^{2+} + H^+ + O_2 \qquad (15)$$

There are two isomers for this structure as well, a seven-coordinate bidentate peroxide and a six-coordinate terminal peroxide. The latter is more stable by 4.1 kcal/mol and is illustrated in Figure 12. In this calculation, the terminal peroxide converged to a weakly antiferromagnetically coupled doublet, as determined by the Mulliken atomic spin densities (Ru, −0.85; O(1), 0.79; O(2), 1.13, Figure 6). A stability calculation revealed that this is indeed the lowest energy configuration. It is most appropriately described as a $d\pi^5$ Ru(III) complex coordinated to triplet oxygen.

Discussion

The results presented here are significant in revealing in complete detail a mechanism for single-site water oxidation catalysis based on $[Ru(tpy)(bpm)(OH_2)]^{2+}$. It is one of a family of single-site water oxidation catalysts including $[Ru(tpy)(bpz)(OH_2)]^{2+}$, $[Ru^{II}(Mebimpy)(bpm)(OH_2)]^{2+}$, $[Ru^{II}(Mebimpy)(bpz)(OH_2)]^{2+}$, and $[Ru^{II}(Mebimpy)(bpy)(OH_2)]^{2+}$, which are promising as long-lived, robust water oxidation catalysts in solution and, as phosphonate-derivatized complexes, on electrode surfaces.[45,46]

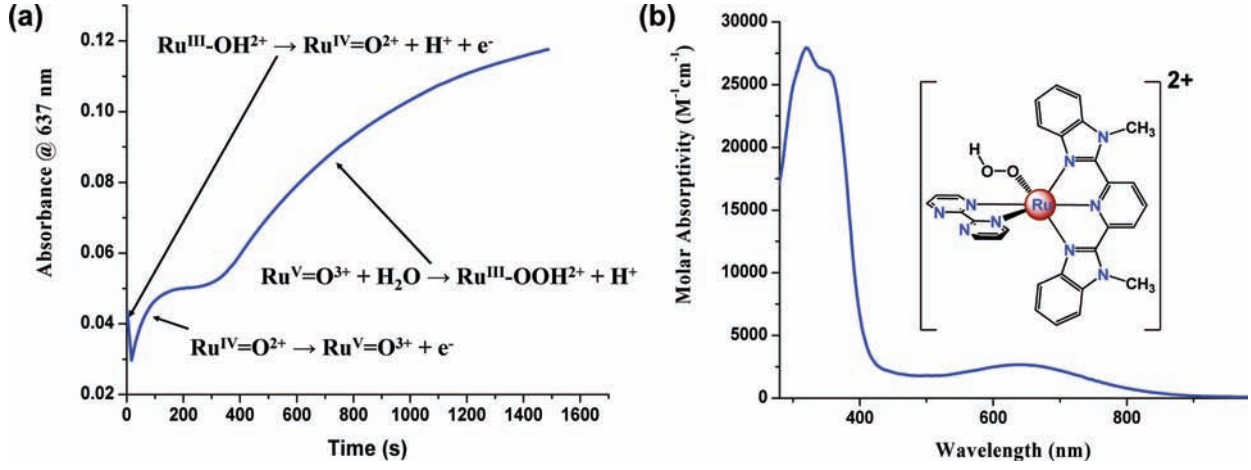

Figure 7. (a) Absorbance−time changes at 637 nm following addition of 3 equiv of Ce(IV) to $[Ru^{II}(Mebimpy)(bpm)(OH_2)]^{2+}$ (5.1×10^{-5} M) in 0.1 M HNO_3 at 25 ± 2 °C. (b) Absorption spectrum of $[Ru^{III}(Mebimpy)(bpm)(OOH)]^{2+}$ in 0.1 M HNO_3.

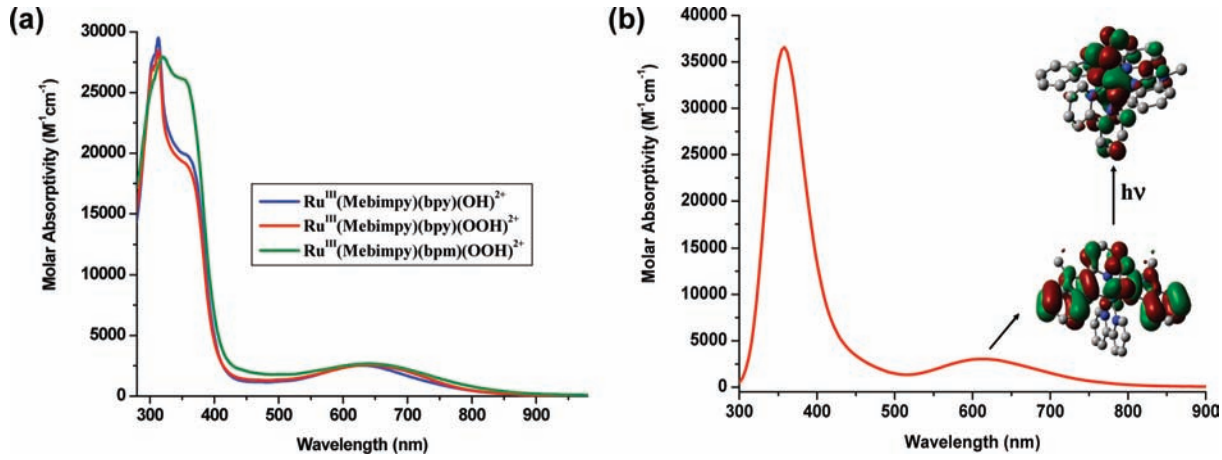

Figure 8. (a) Absorption spectra of $[Ru^{III}(Mebimpy)(bpy)(OH)]^{2+}$, $[Ru^{III}(Mebimpy)(bpy)(OOH)]^{2+}$, and $[Ru^{III}(Mebimpy)(bpm)(OOH)]^{2+}$ in 0.1 M HNO_3 at 25 ± 2 °C. (b) Calculated absorption spectrum for $[Ru^{III}(Mebimpy)(bpy)(OOH)]^{2+}$ in water (TD-DFT) and molecular orbitals associated with the lower energy transition. The solvent was modeled by adding one hydrogen-bound specific water molecule and using IEFPCM for the bulk.

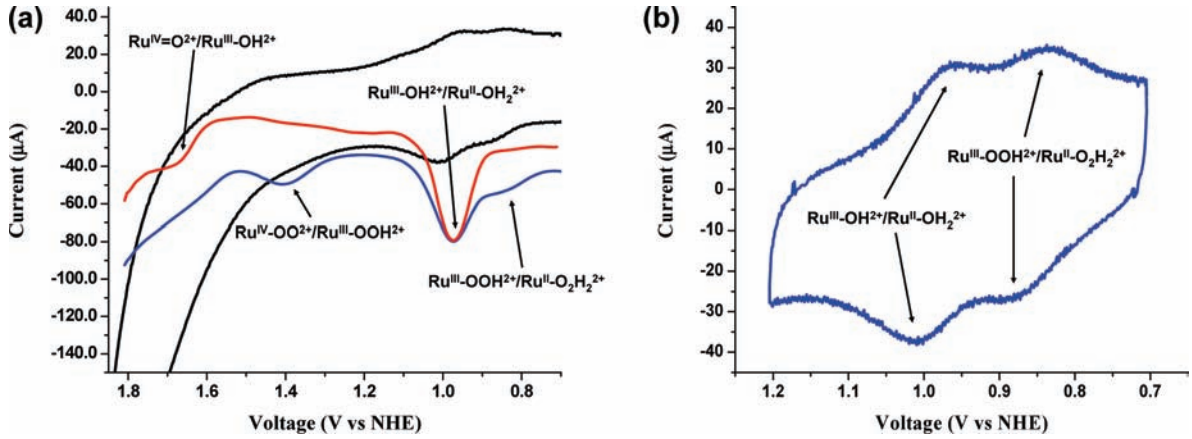

Figure 9. (a) (Black) Cyclic voltammogram for 1.0 mM $[Ru(Mebimpy)(bpm)(OOH)]^{2+}$ in 0.1 M HNO_3 generated in situ by oxidation of $[Ru^{II}(Mebimpy)(bpm)(OH_2)]^{2+}$ by 3 equiv of Ce(IV). Working electrode, glassy carbon; scan rate, 10 mV/s. (Blue) Square wave voltammogram for $[Ru(Mebimpy)(bpm)(OOH)]^{2+}$ in 0.1 M HNO_3. Step, 4 mV; amplitude, 25 mV; frequency, 14 s^{-1}. (Red) Square wave voltammogram for $[Ru(Mebimpy)(bpm)(OH_2)]^{2+}$ in 0.1 M HNO_3. Step, 4 mV; amplitude, 25 mV; frequency, 14 s^{-1}. (b) Cyclic voltammogram for 1.0 mM $[Ru(Mebimpy)(bpm)(OOH)]^{2+}$ in 0.1 M HNO_3 from 0.7 to 1.2 V, showing the $Ru^{III/II}$ waves for $[Ru(Mebimpy)(bpm)(OOH)]^{2+}$ and $[Ru(Mebimpy)(bpm)(OH_2)]^{2+}$. Working electrode, glassy carbon; scan rate, 10 mV/s.

Description of Mechanism. The mechanism in Scheme 1 involves, in sequence, oxidative activation of the $[Ru{-}OH_2]^{2+}$ starting complex by PCET with loss of both protons and electrons, followed by oxidation to $[Ru^{V}{=}O]^{3+}$, O---O bond formation, and further oxidation and O_2 loss through two peroxidic intermediates.

Oxidation of $[Ru^{II}{-}OH_2]^{2+}$ to $[Ru^{IV}{=}O]^{2+}$. Oxidation of $[Ru^{II}(tpy)(bpm)(OH_2)]^{2+}$ occurs directly to $[Ru^{IV}(tpy)(bpm)(O)]^{2+}$. In this coordination environment Ru(III), presumably as $[Ru^{III}(tpy)(bpm)(OH)]^{2+}$, is a kinetic intermediate that is unstable with respect to disproportionation into $[Ru^{IV}{=}O]^{2+}$ and $[Ru{-}OH_2]^{2+}$, with $E^{\circ\prime}(Ru^{III/II}) > E^{\circ\prime}(Ru^{IV/III})$.

This is a consequence of PCET with loss of electrons and protons avoiding charge buildup. This decreases the potential difference between adjacent couples and allows for accumulation of multiple oxidative equivalents at a single site over a narrow potential range.[1,9,39,47] In $[Ru^{II}(tpy)(bpy)(OH_2)]^{2+}$, $E^{\circ\prime}(Ru^{III/II}) < E^{\circ\prime}(Ru^{IV/III})$ by ~100 mV, and $[Ru^{III}(tpy)(bpy)(OH)]^{2+}$ appears as a stable oxidation state.[29] In $[Ru^{II}(tpy)(bpm)(OH_2)]^{2+}$, the back-bonding bpm ligand increases $E^{\circ\prime}(Ru^{III/II})$ above $E^{\circ\prime}(Ru^{IV/III})$, leading to disproportionation.

An analogous observation has been made for $[(bpy)_2(H_2O)Ru^{III}ORu^{III}(OH_2)(bpy)_2]^{4+}$. For the dimer, oxidation of $[(H_2O)Ru^{III}ORu^{III}(OH_2)]^{4+}$ to $[(O)Ru^{V}ORu^{IV}(O)]^{3+}$ occurs through $Ru^{IV}ORu^{IV}$, which is a kinetic intermediate but, like $[Ru^{III}(tpy)(bpm)(OH)]^{2+}$, is unstable toward disproportionation.[6,8,9]

Oxidation of $[Ru^{IV}{=}O]^{2+}$ to $[Ru^{V}{=}O]^{3+}$. Oxidation to $[Ru^{V}{=}O]^{3+}$ occurs at $E^{\circ\prime} = 1.65$ V to create a powerful multielectron oxidant, eq 16a, which is the key intermediate in water oxidation.

$$Ru^{V}{=}O^{3+} + 2H^{+} + 3e^{-} \rightarrow Ru^{II}{-}OH_2^{2+} \qquad E^{\circ\prime} = 1.32\ V \tag{16a}$$

$$Ru^{V}{=}O^{3+} + H^{+} + 2e^{-} \rightarrow Ru^{III}{-}OH^{2+} \qquad E^{\circ\prime} > 1.40\ V \tag{16b}$$

An analogous step occurs in water oxidation by $[(bpy)_2(H_2O)Ru^{III}ORu^{III}(OH_2)(bpy)_2]^{4+}$, which in the final step involves e^{-} oxidation of $[(bpy)_2(O)Ru^{V}ORu^{IV}(O)(bpy)_2]^{3+}$ to the reactive intermediate $[(bpy)_2(O)Ru^{V}ORu^{V}(O)(bpy)_2]^{4+}$.

Reaction of $[Ru^{V}{=}O]^{3+}$ with Water. This is the key O−O bond-forming step with nucleophilic H_2O attack on the highly electron deficient, oxidizing oxo group of $[Ru^{V}{=}O]^{3+}$, eq 17. This reaction occurs with $k = 9.6 \times 10^{-3}\ s^{-1}$. Formation of the peroxidic intermediate is spontaneous, requiring a powerful

oxidant given $E^\circ = -1.78$ V for the H_2O/H_2O_2 couple, $2H_2O \rightarrow H_2O_2 + 2H^+ + 2e^-$. Related O-atom-transfer reactions to sulfides, phosphines, and olefins have been documented for Ru^{IV}=O complexes such as $[Ru^{IV}(tpy)(bpy)(O)]^{2+}$.[39,48−50]

$$Ru^{V}{=}O^{3+} + H_2O \rightarrow Ru^{III}{-}OOH^{2+} + H^+ \qquad (17)$$

An O---O coupling step has also been proposed in water oxidation by water attack on $[(bpy)_2(O)Ru^{V}ORu^{V}(O)(bpy)_2]^{4+}$ to give the peroxide, $[(bpy)_2(OH)Ru^{IV}ORu^{IV}(OOH)(bpy)_2]^{4+}$, which is in acid−base equilibrium with $[(bpy)_2(O)Ru^{V}ORu^{III}(OOH)(bpy)_2]^{3+}$.[5] Blue dimer water oxidation is more rapid by $>10^4$, and it has been suggested that O---O coupling is accompanied by concerted electron−proton transfer with electron transfer to the second Ru site and proton transfer to its O, eq 18. Concerted electron−proton transfer avoids formation of a high-energy isomer of the coordinated peroxide, Ru−O−OH_2.

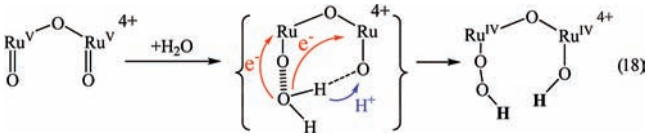

Oxidation of $[Ru^{III}{-}OOH]^{2+}$. Once formed, $[Ru^{III}{-}OOH]^{2+}$ undergoes further one-electron oxidation to $[Ru^{IV}(OO)]^{2+}$. At this point in the catalytic scheme the requirements for water oxidation have been met with loss of $4e^-/4H^+$ and formation of the O−O bond. A related step has been proposed in the final stage of water oxidation in PSII,[1]

$$Mn^{III}OOH^{n+} \xrightarrow{-e^-} Mn^{IV}(OO)^{n+} + H^+$$

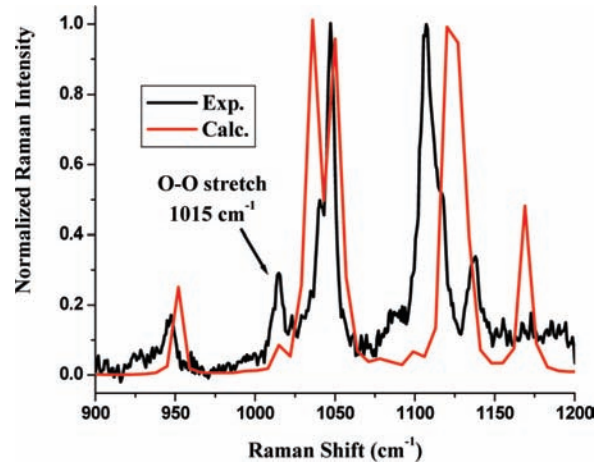

Figure 11. Resonance Raman spectrum for $[Ru^{IV}(Mebimpy)(bpy)(\eta^2\text{-}OO)]^{2+}$ obtained with 442 nm excitation on a Horiba Jobin Yvon LabRam Aramis Microscope spectrometer. The assignment of the band at 1015 cm^{-1} as an O−O stretch is based on the calculated Raman activity spectrum with DFT.

Loss of O_2 from $[Ru^{IV}{-}O_2]^{2+}$. It is ironic that after achieving the stoichiometric requirements for water oxidation in e^-/H^+ loss and O−O bond formation, the rate-limiting step in the catalytic cycle is loss of O_2 from $[Ru^{IV}(OO)]^{2+}$. This is a consequence of the internal electronic structure and nature of the bonding in the intermediate. Decomposition occurs by intramolecular electronic redistribution and charge transfer with release of O_2, eq 19. O_2 loss occurs with $k(25 \pm 2\ ^\circ C) = 7.5 \times 10^{-4}\ s^{-1}$.

$$Ru^{IV}(OO)^{2+} + H_2O \rightarrow Ru{-}OH_2{}^{2+} + O_2 \qquad (19)$$

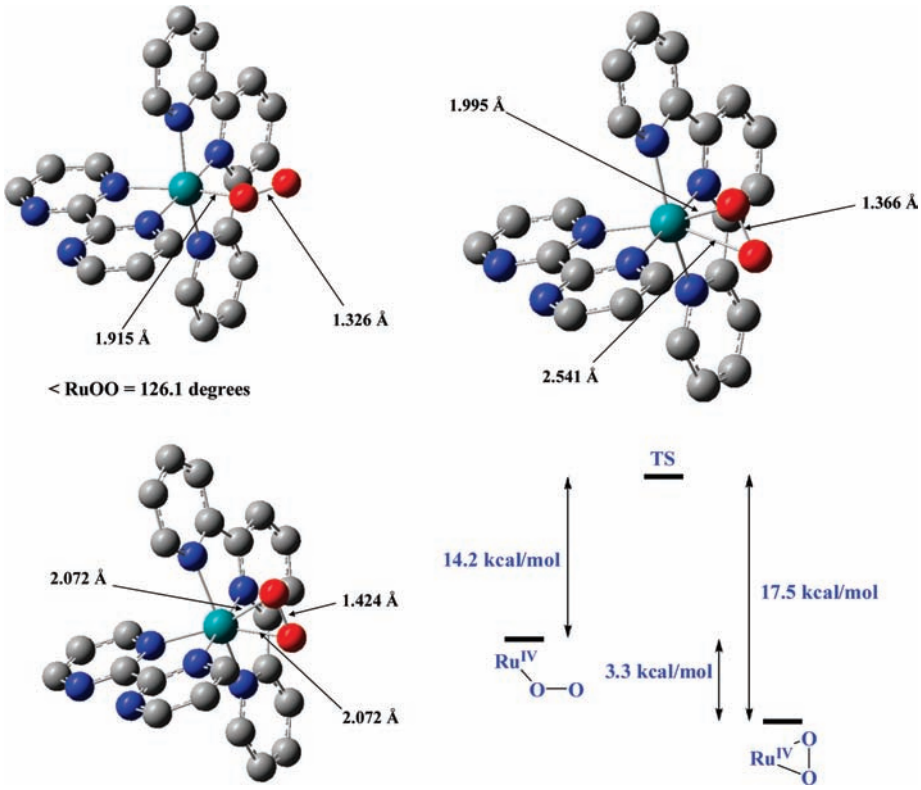

Figure 10. Optimized structures and relative energies (singlets) for the terminal and bidentate Ru^{IV} peroxides and the transition state for their interconversion.

Related behavior is observed in water oxidation by the blue dimer where the peroxidic intermediate, $[(bpy)_2(O)Ru^{V}ORu^{III}(OOH)(bpy)_2]^{3+}$, undergoes rate-limiting O_2 loss, eq 20.

$$(O)Ru^{V}ORu^{III}(OOH)^{3+} + H_2O \rightarrow (HO)Ru^{III}ORu^{III}(OH_2)^{3+} + O_2 \quad (20)$$

Insight is available into the O_2 loss step from the DFT results. From these results the η^2-chelated peroxo intermediate is in equilibrium with a terminal η^1 six-coordinate open form, $[Ru^{IV}—OO]^{2+}$. On the singlet potential energy surface the bidentate form is more stable by 3.4 kcal/mol, with the transition state between them at 17.5 kcal/mol. The pathway for O_2 loss may involve rate-limiting conversion between isomers followed by intramolecular charge transfer and water attack, eq 21a. Low-lying open-shell configurations might play an important role in this step by providing a low-energy pathway for the evolution of triplet oxygen. With a spin−orbit coupling constant of ~1000 cm^{-1} for Ru, intersystem crossing from the closed-shell singlet to the triplet potential energy surface can readily occur.

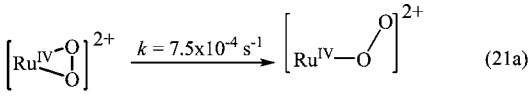

(21a)

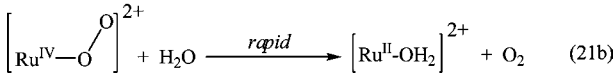

(21b)

Oxidation of $[Ru^{IV}—O_2]^{2+}$ and Release of O_2. $[Ru^{IV}(OO)]^{2+}$ undergoes further oxidation by Ce(IV) in 1.0 M HNO_3 with $k(25 \pm 2\ °C) = 13\ M^{-1}\ s^{-1}$ to give $[Ru^{V}(O_2)]^{3+}$, eq 22. Oxidation facilitates O_2 release with a minimum barrier to O_2 loss. The DFT calculations predict the η^1 peroxo form to be more stable than the η^2 chelate by ~4 kcal/mol, suggesting the mechanism in eq 23.

Scheme 2. Catalytic Cycles in 0.1 and 1.0 M HNO_3

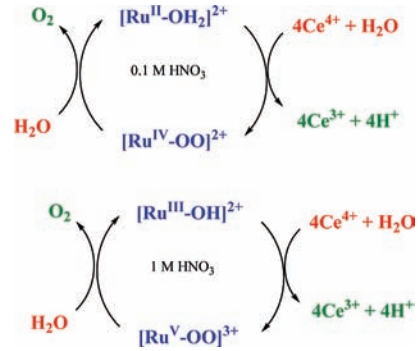

$$Ru^{IV}(OO)^{2+} + Ce(IV) \rightarrow Ru^{V}(O_2)^{3+} + Ce(III) \quad (22)$$

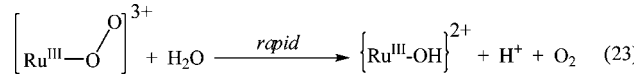

(23)

Catalytic Steady State. The dominant form of the catalyst at the catalytic steady state is $[Ru^{IV}(OO)]^{2+}$ in 0.1 M HNO_3. However, in 1.0 M HNO_3 the enhanced oxidizing strength of the Ce(IV/III) couple increases the rate constant for oxidation of $[Ru^{IV}(OO)]^{2+}$ to $[Ru^{V}(O_2)]^{3+}$. The rate-limiting step in the cycle changes from first-order decomposition of $[Ru^{IV}(OO)]^{2+}$ to further oxidation to $[Ru^{V}(OO)]^{3+}$ followed by rapid O_2 loss.

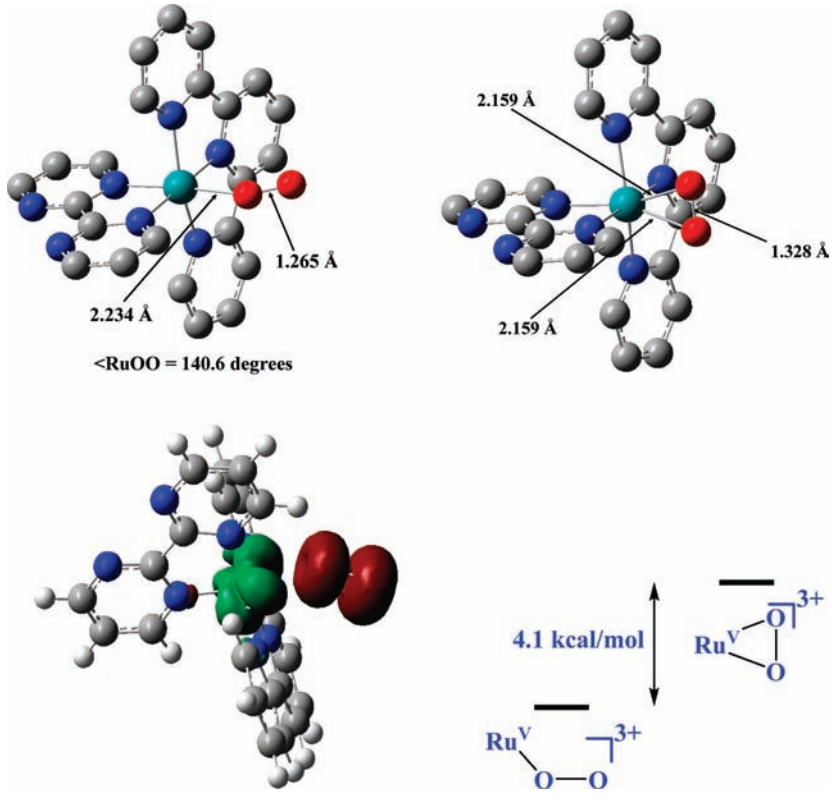

Figure 12. Optimized structures and relative energies (singlets) for the terminal and bidentate Ru^{V} peroxides and Mulliken atomic spin density for the terminal Ru^{V} peroxide.

In 0.1 M HNO_3, the complex cycles between $[Ru—OH_2]^{2+}$ and $[Ru^{IV}(OO)]^{2+}$ (Scheme 2). In 1.0 M HNO_3, the complex cycles between $[Ru^{III}—OH]^{2+}$ and $[Ru^{V}(OO)]^{3+}$.

Conclusions

We describe here a well-defined mechanism for catalytic water oxidation and DFT results on the probable structures of key intermediates. The important features of the mechanism are the following: (1) Stepwise oxidation from $[Ru^{II}—OH_2]^{2+}$ to $[Ru^{V}(OO)]^{3+}$ with exploitation of PCET to avoid charge buildup in the initial $2e^-/2H^+$ oxidation. (2) Further $1e^-$ oxidation to give the powerful oxidant $[Ru^{V}=O]^{3+}$. (3) O---O coupling by water attack on $[Ru^{V}=O]^{3+}$ to give the first of three peroxidic intermediates, $[Ru^{III}—OOH]^{2+}$. (4) Further oxidation to $[Ru^{IV}(OO)]^{2+}$ which slowly releases O_2, giving $[Ru^{II}—OH_2]^{2+}$, and is rate-limiting in the catalytic steady state in 0.1 M HNO_3. (5) In 1.0 M HNO_3, rate-limiting oxidation to $[Ru^{V}(O_2)]^{3+}$ followed by rapid release of O_2, returning the catalytic system to $[Ru^{III}—OH]^{2+}$.

$[Ru(tpy)(bpm)(OH_2)]^{2+}$ and $[Ru(tpy)(bpz)(OH_2)]^{2+}$ (bpz = 2,2′-bipyrazine) are the first members of a family of related single-site and molecular catalysts which appear to utilize a common mechanism for water oxidation.[45] With mechanistic insight available, it is now possible to tune reactivity properties by synthetic variations. This is important in providing a powerful guide for using chemical synthesis to maximize rates, minimize overvoltage in electrochemical and photoelectrochemical reactions, and maximize catalyst stability. By utilizing available synthetic procedures, a means is now available for routinely incorporating water oxidation catalysts at the molecular scale at interfaces, in molecular assemblies, or in nanostructured arrays.

Acknowledgment. Funding by the Chemical Sciences, Geosciences and Biosciences Division of the Office of Basic Energy Sciences, U.S. Department of Energy, Grant DE-FG02-06ER15788, and UNC EFRC: Solar Fuels and Next Generation Photovoltaics, an Energy Frontier Research Center funded by the U.S. Department of Energy, Office of Science, Office of Basic Energy Sciences, under Award DE-SC0001011 is gratefully acknowledged.

Supporting Information Available: Absorption spectra of the ruthenium(II) complexes in their aquo and hydroxy forms; complete ref 17. This material is available free of charge via the Internet at http://pubs.acs.org.

JA904906V

(45) Concepcion, J. J.; Jurss, J. W.; Brennaman, M. K.; Hoertz, P. G.; Patrocinio, A. O. T.; Murakami Iha, N. Y.; Templeton, J. L.; Meyer, T. J. *Acc. Chem. Res.* **2009**, *42*, 1954–1965.
(46) Concepcion, J. J.; Jurss, J. W.; Hoertz, P. G.; Meyer, T. J. *Angew. Chem., Int. Ed.* **2009**, *121*, 9637–9640.
(47) Huynh, M. H. V.; Meyer, T. J. *Chem. Rev.* **2007**, *107*, 5004–5064.
(48) Roecker, L.; Dobson, J. C.; Vining, W. J.; Meyer, T. J. *Inorg. Chem.* **1987**, *26*, 779–781.
(49) Moyer, B. A.; Meyer, T. J. *J. Am. Chem. Soc.* **1978**, *100*, 3601–3603.
(50) Seok, W. K.; Meyer, T. J. *Inorg. Chem.* **2004**, *43*, 5205–5215.
(51) Bondareva, T. N.; Stromberg, A. G. *Zh. Obshch. Khim.* **1955**, *25*, 666–671.